# Crustal conductivity footprint of the Miocene porphyry copper polymetallic deposits in the Gangdese metallogenic belt, Tibetan Plateau

Sheng, Yue; Jin, Sheng; Comeau, Matthew J.; Hou, Zengqian; Yin, Yaotian; Zhang, Letian; Wei, Wenbo; Ye, Gaofeng

# Crustal conductivity footprint of the Miocene porphyry copper polymetallic deposits in the Gangdese metallogenic belt, Tibetan Plateau

Yue Sheng [a], Sheng Jin [a,b,*], Matthew J. Comeau [c], Zengqian Hou [d,*], Yaotian Yin [a,b], Letian Zhang [a,b], Wenbo Wei [a,b], Gaofeng Ye [a,b]

[a] *School of Geophysics and Information Technology, China University of Geosciences, Beijing 100083, China*
[b] *Key Laboratory of Intraplate Volcanoes and Earthquakes (China University of Geosciences, Beijing), Ministry of Education, Beijing 100083, China*
[c] *Department of Geoscience and Engineering, Delft University of Technology, 2628 CN Delft, the Netherlands*
[d] *Key Lab of Continental Tectonics and Dynamics, Institute of Geology, Chinese Academy of Geological Sciences, Beijing 100037, China*

ARTICLE INFO

ABSTRACT

New evidence worldwide has linked the surface locations of mineral deposits and their crustal-scale electrical conductivity footprint. We examine the relationship between the Gangdese Miocene porphyry copper deposits, Tibetan Plateau, and the electrical conductivity signature from a three-dimensional model generated from 311 magnetotelluric measurements. The distribution of electrical resistivity throughout the crust and the conductance within the mid-lower crust (depth range of 25–70 km) is analyzed. The results clearly show that the large and ultra-large Miocene porphyry copper deposits coincide spatially with conductive zones and areas of very-high conductance (>10,000S) in the mid-lower crust. Computations are undertaken to determine the influence of water-bearing silicate melts and alkali-bearing ($Na^+$ and $K^+$) fluids on conductivity. Based on this, the bulk conductivity is interpreted to be caused by a system of alkali-rich volatile-rich partial melt. The alkali-rich volatile-rich magmatic-hydrothermal fluids facilitate the migration and concentration of metal ions originating in deep areas. The volumes necessary are much less than partial melt alone and can thus help to reconcile large conductivity variations with small seismic velocity variations. The electrical structure indicates the magma source area of anatexis in the lower crust, a multi-stage magmatic system with large mid-crustal and small upper-crustal magma reservoirs, and complex pathways related to rift zones. We determine that the conductive zones in the mid-lower crust have an influence on the development of the mineralization and the location of the mineral belt.

## 1. Introduction

Porphyry copper deposits (PCDs) can be formed in accretion-type orogenic belts related to the subduction of oceanic plates, in collision-type orogenic belts related to continent–continent convergence, in continental orogenic belts related to continental subduction, and in the reactivated or destroyed craton interiors and craton margins (e.g., Hou et al., 2020). In contrast to the understanding of PCDs in arc-magmatic backgrounds, there has been much less work and consensus on the formation and evolution of PCDs in non-arc magmatic backgrounds (especially in orogenic belts).

The Gangdese porphyry copper polymetallic belt, Tibetan Plateau, is a typical example of a porphyry copper deposit formed in a collision-type orogenic belt. Intriguingly, obvious differences are observed in

the crustal structure, mantle features, and the thermal state between the western and eastern Gangdese metallogenic belt, taking longitude 88°E as the boundary, which is likely responsible for differences in the mineralization (Hou et al., 2015, 2023; Wang et al., 2015, 2018). Miocene porphyry copper polymetallic deposits (MPCDs), such as Zhunuo, Jiru (including Eocene mineralization), Tinggong, Qulong, and Jiama (listed west to east), have formed in the southern Lhasa terrane, following magmatic activity in the post-collision stage (Hou et al., 2015; Zhu et al., 2019). The ore-forming Miocene adakitic granitoids are interpreted to be derived from remelting of the juvenile lower crust with metal fertilization caused by previous subduction-related modification during the Miocene (Hou et al., 2015).

Sr-Nd-Hf isotopic results show that most the MPCDs have a close spatial relationship with the juvenile lower crust. In contrast, the

Zhunuo deposit formed outside the extent of the Jurassic arc and in the western boundary of the juvenile lower crust (Hou et al., 2015). Previous studies have been carried out to examine the origin of the ore-bearing magma in this area, the evolution of the magmatic fluids, the source and enrichment process of the metallogenic elements (e.g., copper, gold and molybdenum), and the characteristic oxygen fugacity (Yang et al., 2015; Hou et al., 2015, 2020; Wang et al., 2018, 2021; Zheng et al., 2018, 2020; Yang & Fu, 2020; Zhang et al., 2022). Based on geochemical and geophysical data, Hou et al. (2023) described three key metallogenic factors of the MPCDs: a torn slab subducted at moderate angle, prior fertilization of the lower crust with Cu, and *trans*-lithospheric vertical structures for magma ascent. However, geophysical research is an important component that is required to image the subsurface and to better understand deep processes and physical states.

Magnetotellurics (MT) is a passive electromagnetic geophysical method. It probes the subsurface electrical structure by measuring the time variation of natural electric and magnetic fields at the Earth's surface. It is well-suited to identify anomalous bodies of high conductivity, high temperature, and strong rheology contrasts (e.g., Unsworth et al., 2005; Wei et al., 2009). Furthermore, electrical signatures can be preserved over (geological) time, until a new and significant (tectonic or geodynamic) event overprints the signatures (e.g., Hill et al., 2021; Wise & Thiel, 2019; Di et al., 2023). The electrical structure is useful for understanding the whole mineral system because it can link lithospheric architecture, deep source regions of metals and fluids, fluid-flow

pathways, and the emplacement locations of discrete mineral deposits −- helping to advance new exploration strategies for the future. Previous studies have successfully exploited the MT technique to gain insights on the relationship between high conductivity anomalies and the imprints of the formation of mineral ore deposits, in regions as diverse as China, Australia, Canada, and Mongolia (e.g., Heinson et al., 2018; Yin et al., 2021; Lü et al., 2021; Hill et al., 2021; Zhang et al., 2021, 2023; Vadoodi et al., 2021; Sheng et al., 2022; Comeau et al., 2022).

Previous research emphasized a strong link between MPCDs and Miocene N-S-trending rifts (e.g., Yadon-Gulu rift) in the Lhasa terrane (Wang et al., 2015, 2021). The work presented here focuses on the area between longitudes 82°E and 93°E in the southern Lhasa terrane and uses an array of MT measurements to generate a 3-D model of the electrical structure. This model has better coverage of the MPCDs and better resolution than other local studies because it includes new data in some key regions (cf. Jin et al., 2022). Based on the explanations for the anomalous conductive zones in the crust and their formation mechanisms, the relationship between the deep electrical structure and the metallogenic dynamics of the MPCDs from an overall perspective across this large region will be sought, for the first time — which advances understanding of deep processes in the development of MPCDs and, more generally, of the link between deep sources and pathways of ore-forming fluids within mineral systems worldwide.
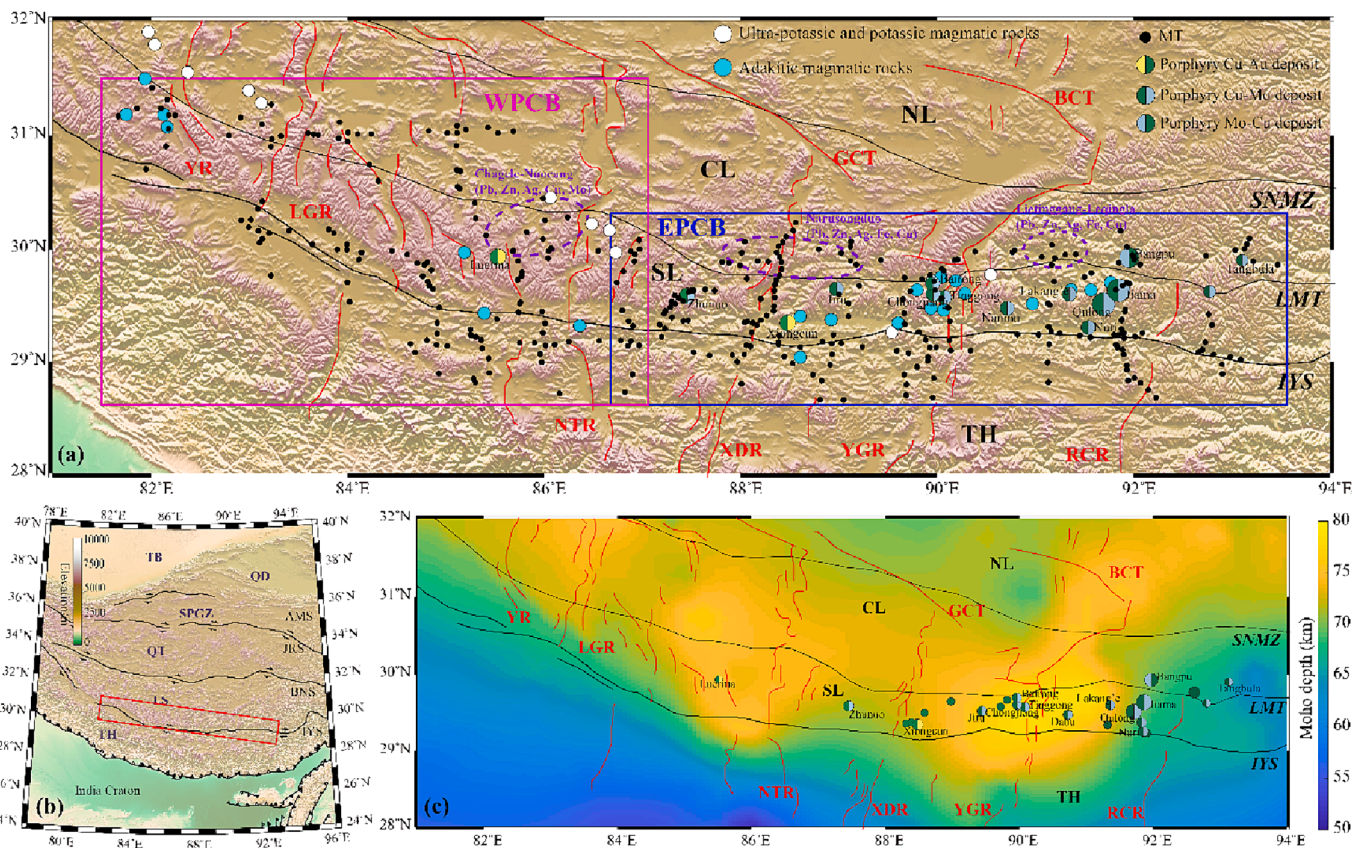


**Fig. 1.** Map of the study area. (a) The locations of magnetotelluric measurements (black dots) and major tectonic structures (red = rifts, black = terranes; see acronyms below). For modelling purposes, the study area is divided into two regions (boxes). The main ore deposits are indicated (derived from Hou et al., 2015; circle symbols, see legend), as are adakitic (blue dots) and potassic magmatic rocks (white dots). (b) Topography of the Tibetan Plateau and its adjacent areas. The red rectangle outlines the study area. (c) Moho depth (Li et al., 2013). Granite-related Pb-Zn deposits and skarn Fe-Cu deposit (Narusongduo, Chagele, and Lietinggao-Leqingla) are marked with a purple dashed circle. TH: Tethys-Himalaya; LS: Lhasa terrane (SL, CL, NL: Southern, Central, Northern Lhasa terrane); QT: Qiangtang terrane; SPGZ: Songpan- Ganzi terrane; QD: Qaidam basin; TB: Tarim basin; IYS: Indus-YarlungZangbo suture; LMF: Luobadui- Milashan Fault; SNMZ: Shiquan River-Nam Tso Mélange Zone; BNS: Banggong- Nujiang suture; JRS: Jinsha River suture; AMS: Animaqing suture; RCR: Riduo-Cuona Rift; YGR: Yadong-Gulu Rift; XDR: Xainza-Dinggye Rift; NTR: Niyima-Tingri Rift; LGR: Longgar Rift. YR: Yari Rift. (For interpretation of the references to colour in this figure legend, the reader is referred to the web version of this article.)

## 2. Data and inversion

### 2.1. Data collection and analysis

The study area encompasses a region in the southern Lhasa terrane (Fig. 1), between longitude 82°E and 93°E. It consists of 311 MT measurements, many of which were acquired by China University of Geosciences (Beijing). Because the dataset includes some older data from the INDEPTH project (e.g., Wei et al., 2001; Unsworth et al., 2005) and some newly-acquired data, it is denser than the datset used by Jin et al. (2022) and covers more important regions (e.g., Zhunuo, Bairong, and Qulong-Jiama districts). High-quality MT data were collected with Phoenix Canada MTU-5 instruments with a period range of 0.003–3,000 s and a recording time of 24 h. Five components of the time-varying electromagnetic field (Ex, Ey, Hx, Hy, and Hz, where x, y, and z are the South-North, East-West, and vertical directions) were recorded and were optimized using the remote reference method. The time series data were transformed into the frequency domain, after which frequency-dependent transfer functions were computed with a statistically robust algorithm (Egbert, 1997).

The phase tensor, shown by an ellipse, can provide information on the data dimensionality (Caldwell et al., 2004; Booker et al., 2013). Because the phase tensor is not easily affected by 3-D distortion, the ellipse long axis can determine the strike direction of the MT data conveniently. The skew angle β is used to analyze the dimensionality and whether the assumption of 2-D structure is reasonable (Fig. 2). When β is equal or similar to zero, the MT data exhibit ideal one-dimensionality or two-dimensionality; when β is nonzero, the MT data exhibit three-dimensionality. We use a threshold value (generally 3°) of the absolute value of β (|β|) (Caldwell et al., 2004). The larger the |β| changes, the stronger the three-dimensionality exhibited (Booker et al., 2004). Based on the values of |β| for all the MT stations, and the distribution of MT stations, using a 3-D inversion is preferred.

### 2.2. Three-dimensional (3-D) inversion

A 3-D modeling approach was undertaken with the ModEM 3-D inversion algorithm (Egbert & Kelbert, 2012; Kelbert et al., 2014). Because of the irregular shape of the study area, it is divided into two subregions (WPCB and EPCB; Fig. 1a) in order to decrease the grid size and the computational load. In order to smooth the transition between both models, we define a central overlapping region (near longitude 87°E) where the same measurements are used in both models. The starting model, for both subregions, was a uniform 100 Ω·m half space. The modeling grid uses a horizontal cell size of 4 km; the thickness of the first layer is 50 m and increases at a rate of 1.1 in the core area and 1.5 in the outer area. The modeling grids are 70 × 195 × 73 (N-S, E-W, and vertical) (with seven air layers) for EPCB and 104 × 158 × 73 for WPCB. The 3-D inversion uses the total impedance tensor data (**Z**; four complex components) for 6 periods in each decade, logarithmically spaced between 0.01 and 3,000 s (34 frequency points in total). Error floors were 5 % of sqrt(|Zxy * Zyx|) for Zxy and Zyx impedance components and 10 % of sqrt(|Zxy * Zyx|) for Zxx and Zyy. Note that 5 % error on the impedance tensor is equivalent to approximately 10 % on the apparent resistivity component and 2.86° on the phase component. The final normalized-root-mean-square (nR.M.S.) misfit of the model was reduced from 22.5 to 1.96 for WPCB and from 23.49 to 1.88 for EPCB.

The nR.M.S. values of half of the MT stations are less than 2, some stations have values ranging from 2 to 3, and several stations have values above 3 (Fig. 3). To analyze the fit of the model response to the observed data, the apparent resistivity and impedance phase for both regions are examined with pseudo-slices for one period in each order of magnitude (T = 1 s, 10 s, 100 s, and 1,000 s) (Figs. 4 and 5). The


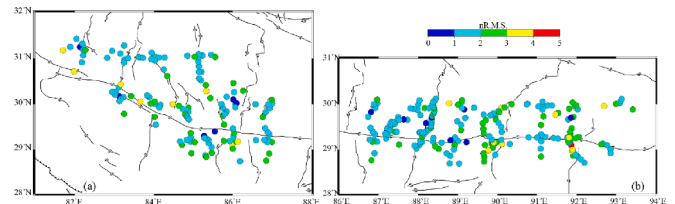
**Fig. 3.** Site-by-site nR.M.S. misfit for the models in the (a) WPCB and (b) EPCB subregions.
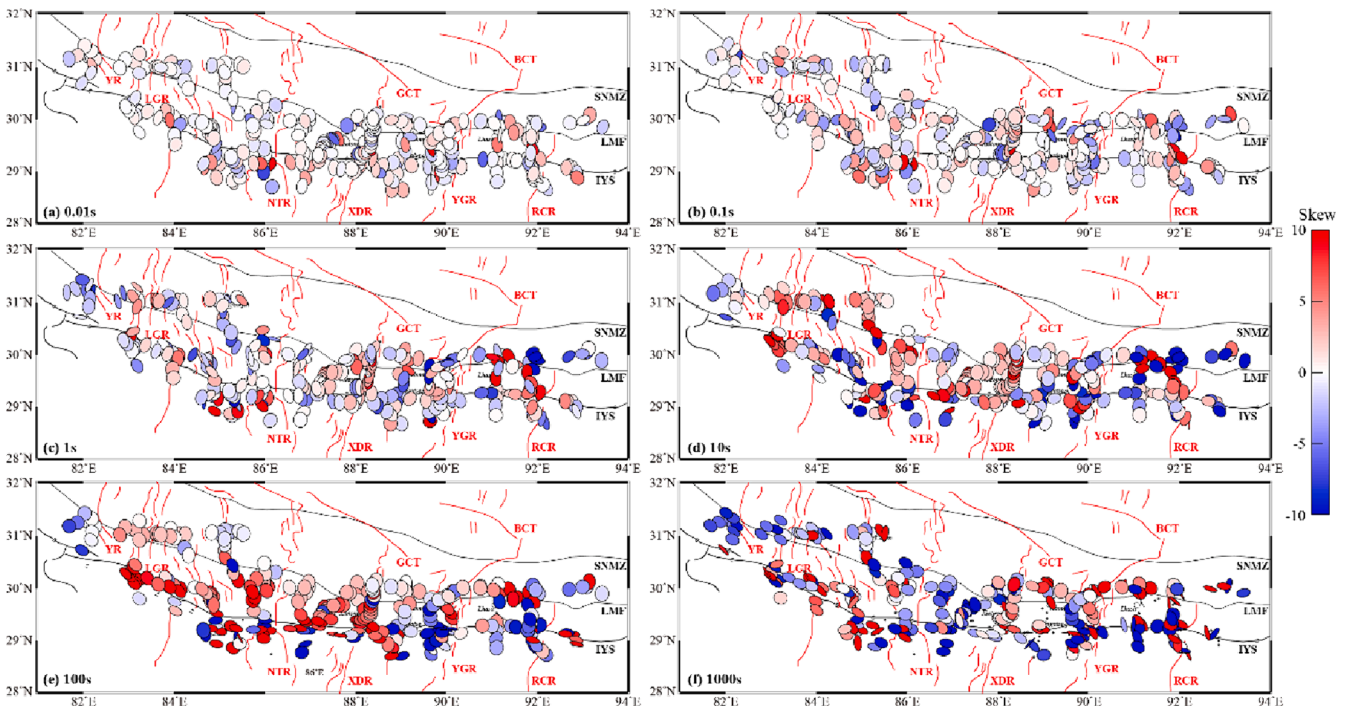


**Fig. 2.** Phase tensor maps for periods of (a) 0.01 s, (b) 0.1 s, (c) 1 s, (d) 10 s, (e) 100 s, (f) 1000 s. Refer to Fig. 1 for labels.
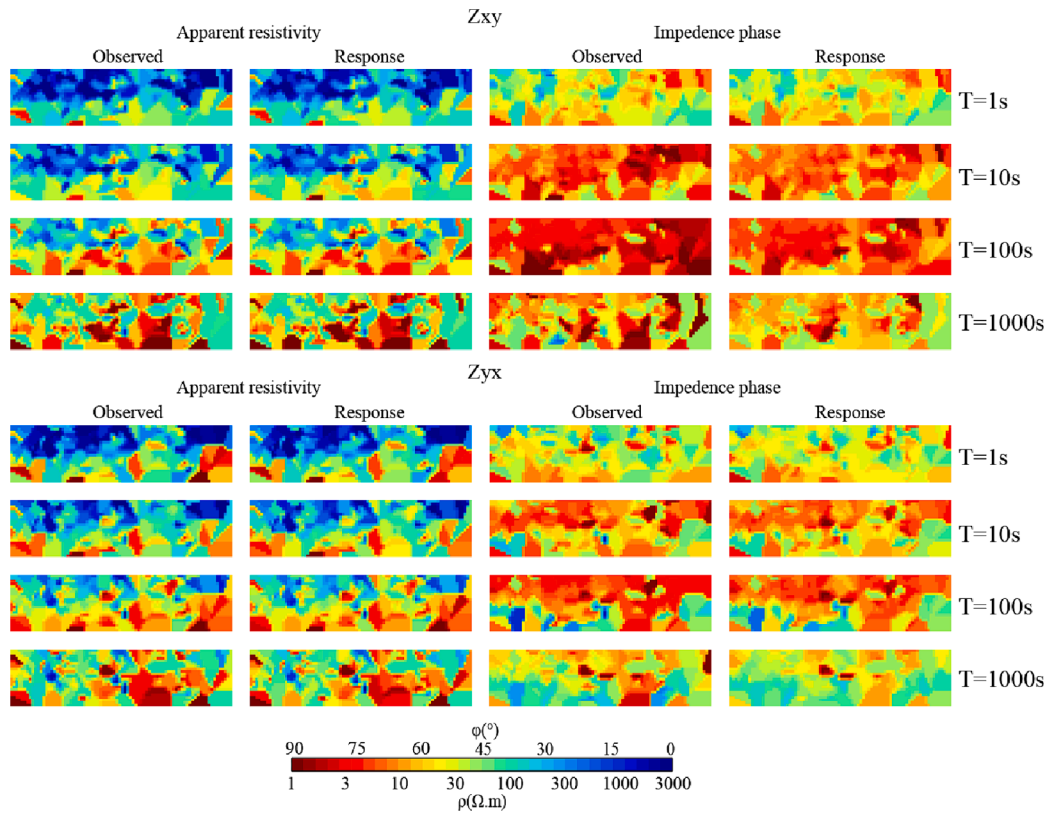
**Fig. 4.** The observed apparent resistivity and impedance phase compared to the 3-D model response for sub-region EPCB, shown with horizontal pseudo-slices for periods from T = 1 s to T = 1,000 s.

comparison shows good agreement for periods of less than 100 s, although several stations have differences in the impedance phase. The apparent resistivity is also well modelled for long period data (1,000 s) although the impedance phase appears to be sometimes inconsistent. Above all, the site-by-site nR.M.S. distribution and the comparison between observed data and model response show that the data fit is not biased and that the given model adequately fits the MT data.

## 3. Results

### 3.1. Sensitivity test and model combination

The model results for both separate subregions are shown in Fig. 6. The models can define the depth to the top of conductive zones; however, they are not sensitive to the bottom (i.e., it's thickness) because equivalent models can give similar integrated conductance. Therefore, sensitivity tests must be carried out to verify the reliability of the main conductive layers. For example, the vertical extension of the imaged conductors EPCB-C1, EPCB-C2, EPCB-C3, WPCB-C1, WPCB-C2, WPCB-C3, and WPCB-C4 (Figures S1–S7). We took the following strategy: we extended those features to greater depths, for example from 70 km to 50 km, compared to the original model, by adding a conductive block (1 Ω·m). The changes in the model are assessed by examining the change in nR.M.S. for all sites, and especially those above or near the corresponding conductors. New response data are computed through forward modeling, and the site-by-site RMS misfit distributions are plotted. These tests indicate that the MT data are sensitive to the electrical structures beneath all the main conductors, and the extension to depths of 70 km is reliable (i.e., the entire crust).

Then, we employed the approach of Jin et al. (2022) to combine two models derived from separate regions to solve the challenge of inverting a large area and many data points. The n.R.M.S. misfit of the shared MT stations (overlapping region near longitude 87°E) is less than 3, the

difference between two corresponding stations is not large (Fig. 6), and the separate 3-D electrical models themselves (WPCB and EPCB) in the vicinity of the shared line are generally similar with only small differences (Fig. 6). The n.R.M.S. misfit of the shared MT stations (between sub-regions) can be computed from a weighted-average based combination of the misfit of the two separate models, with the minimum misfit having the maximum weight. The weight factors are defined as

$$weight_1 = \frac{nR.M.S._{(WPCB)}}{nR.M.S._{(WPCB)} + nR.M.S._{(EPCB)}} \quad (1)$$

and

$$weight_2 = \frac{nR.M.S._{(EPCB)}}{nR.M.S._{(WPCB)} + nR.M.S._{(EPCB)}} \quad (2)$$

and

$$nR.M.S._{(total)} = weight_1 \times nR.M.S._{(EPCB)} + weight_2 \times nR.M.S._{(WPCB)} \quad (3)$$

The preferred electrical resistivity models for regions WPCB and EPCB use the same lambda parameter in the inversion, and the combined model in the shared region is observed to be reasonably smooth and continuous (Fig. 7).

### 3.2. Description of the conductive features

At depths of less than 20 km, the electrical structure shows a series of isolated conductive zones embedded in large-scale resistive zones (Fig. 7). These large-scale zones are indicative of the volcanic strata (e. g., Paleogene Linzizong volcanic rocks and Cretaceous-Eocene Gangdese granitoids). At depths of more than 30 km, in the mid-lower crust, large-area conductive zones are observed (Fig. 7), and the conductivity of these zones typically decreases with depth. Furthermore, it is observed that the discrete conductive zones in the upper crust have a good connection to the conductive zones below in the mid-lower crust.
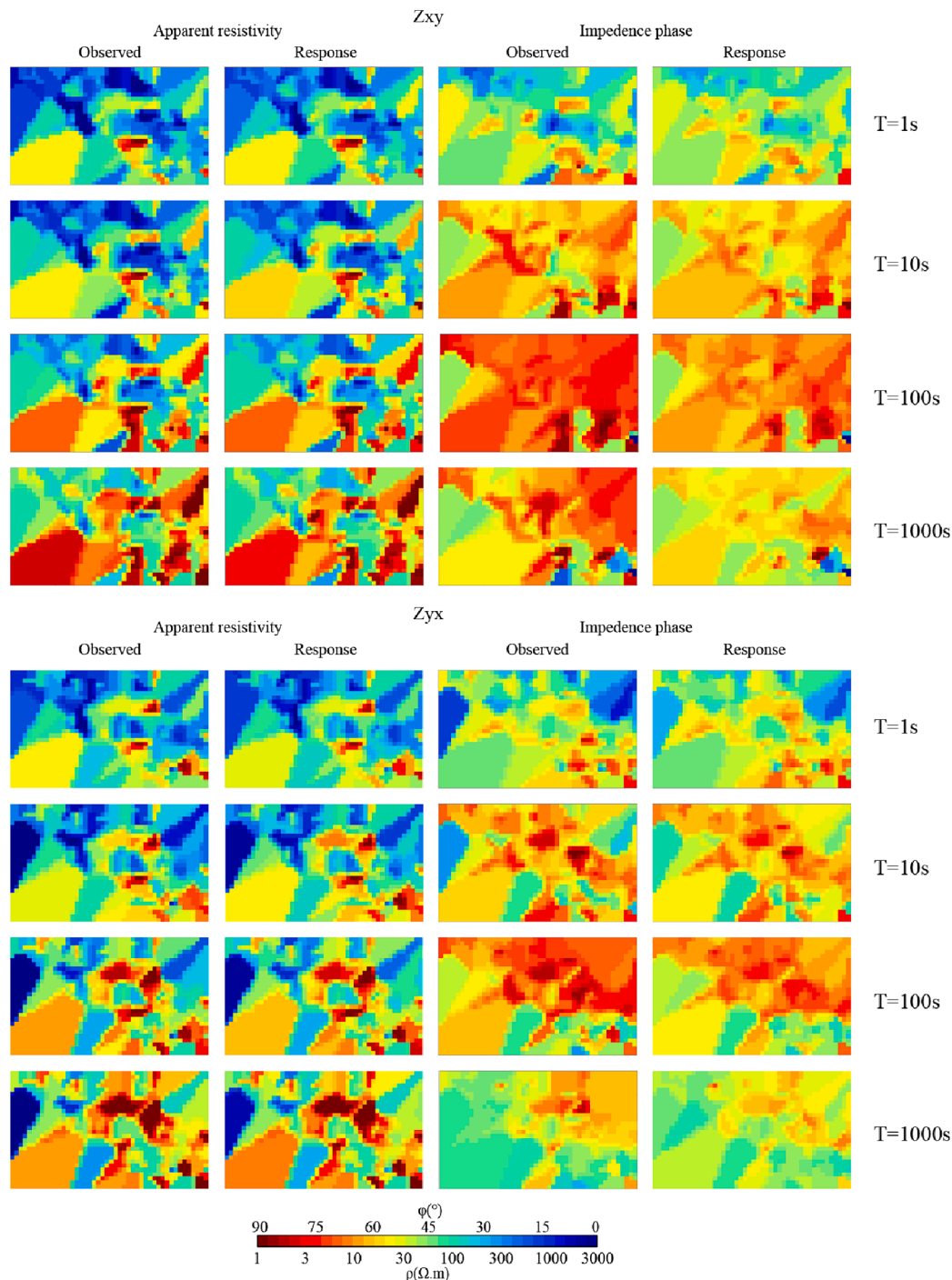
**Fig. 5.** The observed apparent resistivity and impedance phase compared to the 3-D model response for sub-region WPCB, shown with horizontal pseudo-slices for periods from T = 1 s to T = 1,000 s.

Besides the distribution of conductive anomalies at different depths, the conductance (product of conductivity and thickness, units of siemens [S]) of different layers is also an important parameter, which takes the volume effect of the MT method into account. Based on the spatial distribution of conductive features and the average thickness of the upper, middle, and lower crust, the conductance at depths of 25–70 is calculated (Fig. 8).

Examining the features imaged in the electrical resistivity model in combination with the conductance maps, four main zones (marked A1, A2, A3, and A4) are identified in the mid-lower crust of the southern Lhasa terrane that have a high conductivity and a very high

conductance, with a conductance of >10,000 S (Fig. 8). Several other conductive zones (B1, B2, B3, B4, and B5), are characterized by a conductance of >5,000 S (Fig. 8), which is still notably high. In comparison, many other regions in the southern Lhasa terrane are characterized by a conductance of <2,000 S. To provide a comparison, the conductance is computed at depths of 10–25 km (upper crust), 25–45 km (middle crust), and 45–70 km (lower crust) (Fig. S8). Note that the conductance at depths of 25–70 km (middle-lower crust) is the sum of conductance at depths of 25–45 km and 45–70 km. The conductive zones A1, A2, A3, and A4 at depths of 25–70 km (Fig. 8) correspond mostly with the strong high-conductance features in the middle crust

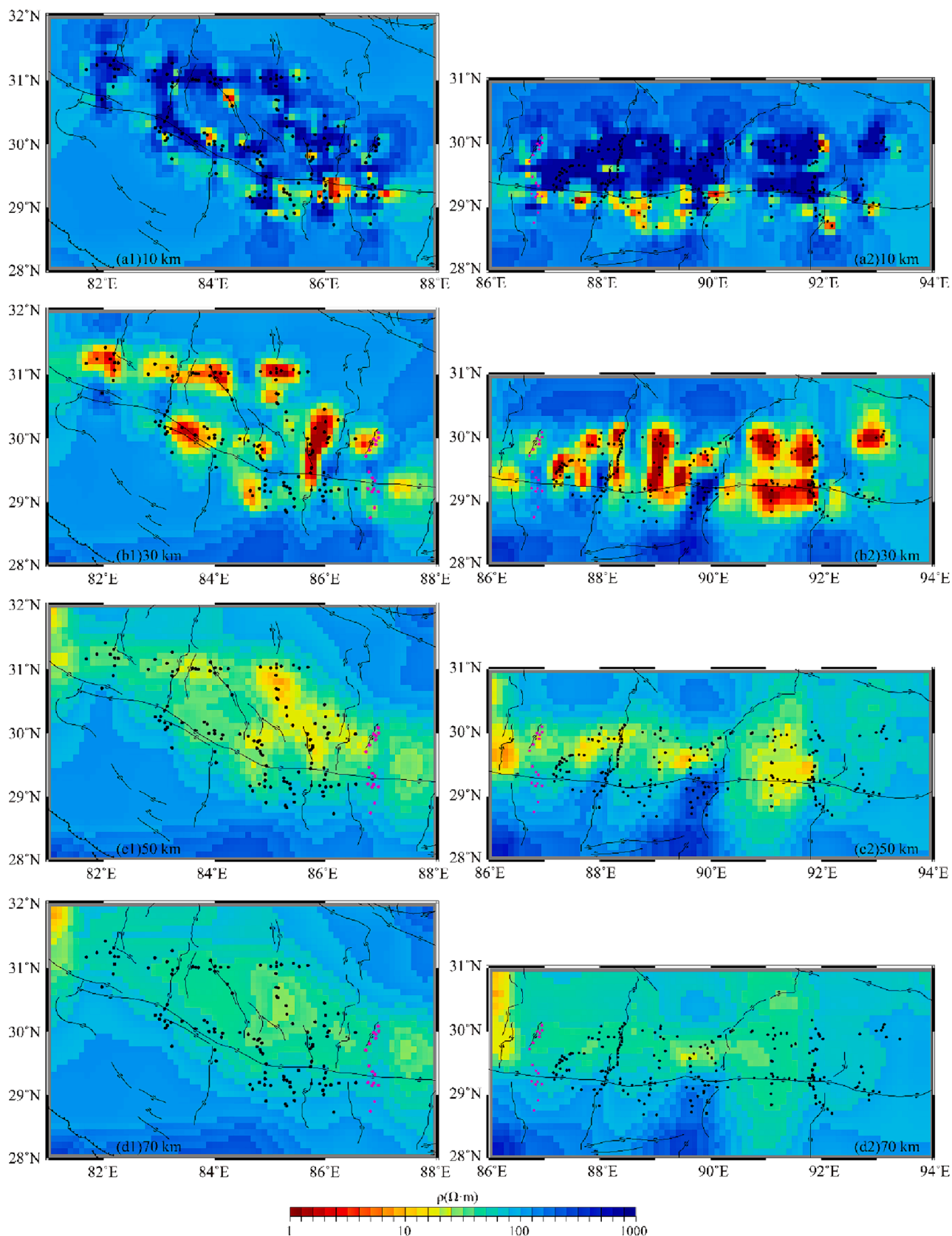**Fig. 6.** Electrical resistivity models for each subregion, WPCB (a1-d1) and EPCB (a2-d2), shown for representative depths of 10, 30, 50 and 70 km. The locations of magnetotelluric measurements are black dots and the shared measurements between regions are the pink dots. (For interpretation of the references to colour in this figure legend, the reader is referred to the web version of this article.)
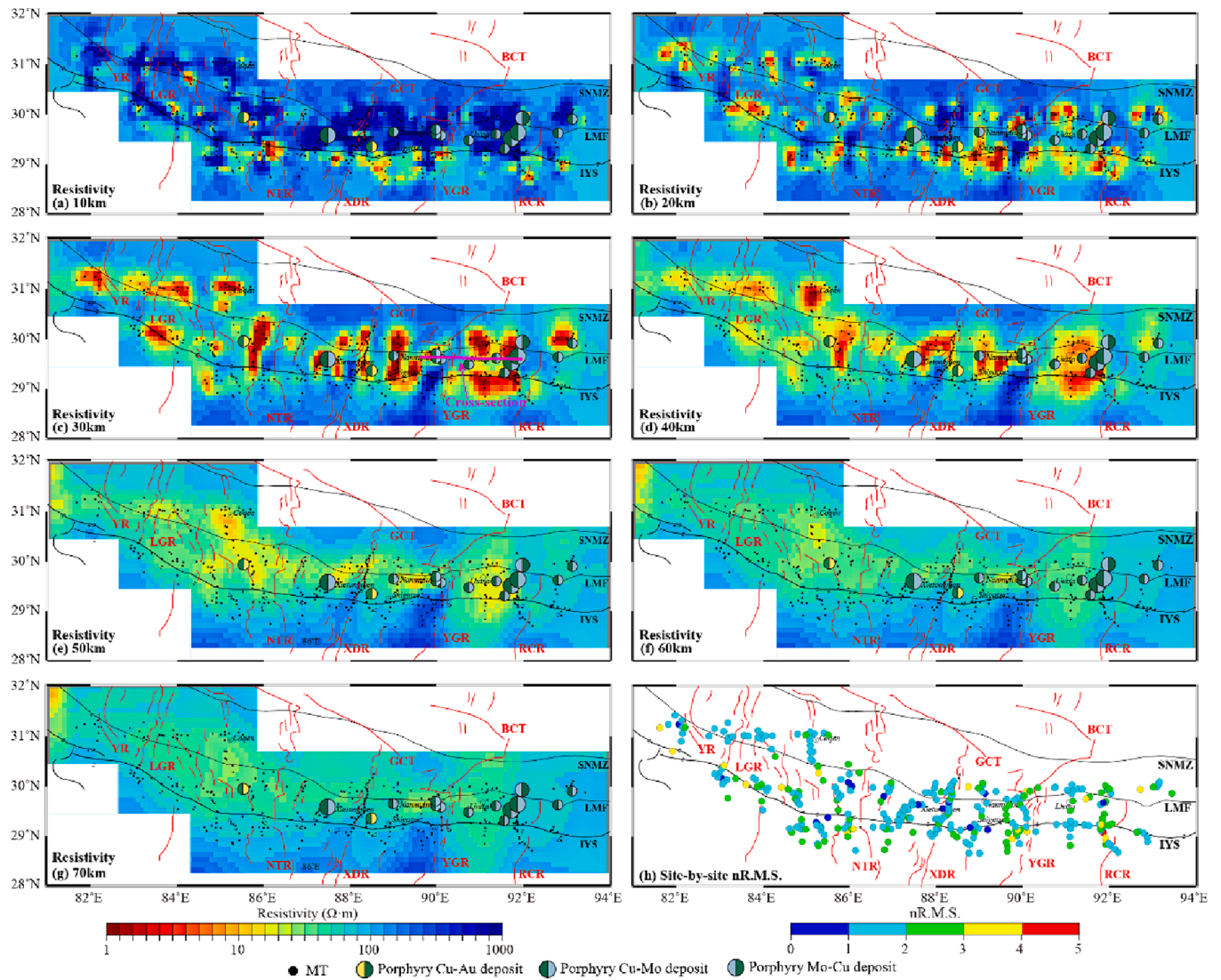
**Fig. 7.** 3-D electrical resistivity model. (a)-(g) Horizontal slices of the electrical resistivity. Labels as in Fig. 1. (h) Site-by-site nR.M.S. misfit of the 3-D inversion. Pink line in 7c is shown in Fig. 6a. Refer to Fig. 1 for labels. (For interpretation of the references to colour in this figure legend, the reader is referred to the web version of this article.)

(25–45 km; Fig. S8b), in addition to those in the lower crust (45–70 km; Fig. S8c). Considering the volume effect of the MT method and the results of the sensitivity tests, the conductive zones A1, A2, A3, and A4 are considered to be crustal scale. Conductance at depths of 45–70 km (lower crust) in the conductive zones B1, B2, B3, B4, and B5 is lower than that in the conductive zones A1, A2, A3, and A4, and contributes little to the conductance in the range of 25–70 km depth.

## 4. Constraining volume fraction of melts and fluids from the electrical resistivity model

### 4.1. Volume fraction of silicate melts

Partial melting and aqueous (or salt-bearing) fluids are two factors that can explain crustal conductive zones (Unsworth et al., 2005; Wei et al., 2009; Sheng et al., 2022). In the study area, the temperature in the middle-lower crust is reported to be > 650 °C (Sun et al., 2013) and the pressure is estimated to be 0.5–2 GPa based on the simple relationship of pressure and density (Sun et al., 2013; Bai et al., 2013). Therefore, based on the interpretation of experimental results (e.g., Naif et al., 2021, and others), it is possible to have the occurrence of silicate melts with

aqueous fluids under the right pressure–temperature conditions. The Hashin–Shtrikman upper bound (HS+; Equation 1), which can be thought of as a model of resistive (rock grain) inclusions within a conductive (melt/fluid) medium and thus allows for full interconnetivity of the conductive phase, is used to estimate the volume fraction of the conductive phase (Hashin & Shtrikman, 1962).

$$\sigma_{HS_+} = \sigma_{melt} \frac{3\sigma_{solid} + 2V(\sigma_{melt} - \sigma_{solid})}{3\sigma_{melt} + V(\sigma_{melt} - \sigma_{solid})} \tag{1}$$

where $\sigma_{HS_+}$ is the bulk conductivity, $\sigma_{melt}$ is the melt/fluid conductivity, $\sigma_{solid}$ is the conductivity of solid matrix, and $V$ is the fraction of the melt phase.

Based on the main volcanic rocks distributed in the southern Lhasa terrane, we use the empirical relationships of conductivity, water content, temperature, and pressure of andesitic and rhyolitic melts from Guo et al. (2017) and Guo et al. (2016). The equations are written as:

$$\log \sigma_{melt}^{andesitic} = 5.23 - 0.56w^{0.6} - \frac{8130.4 - 1462.7w^{0.6} + (581.3 - 12.7w^2)P}{T}$$
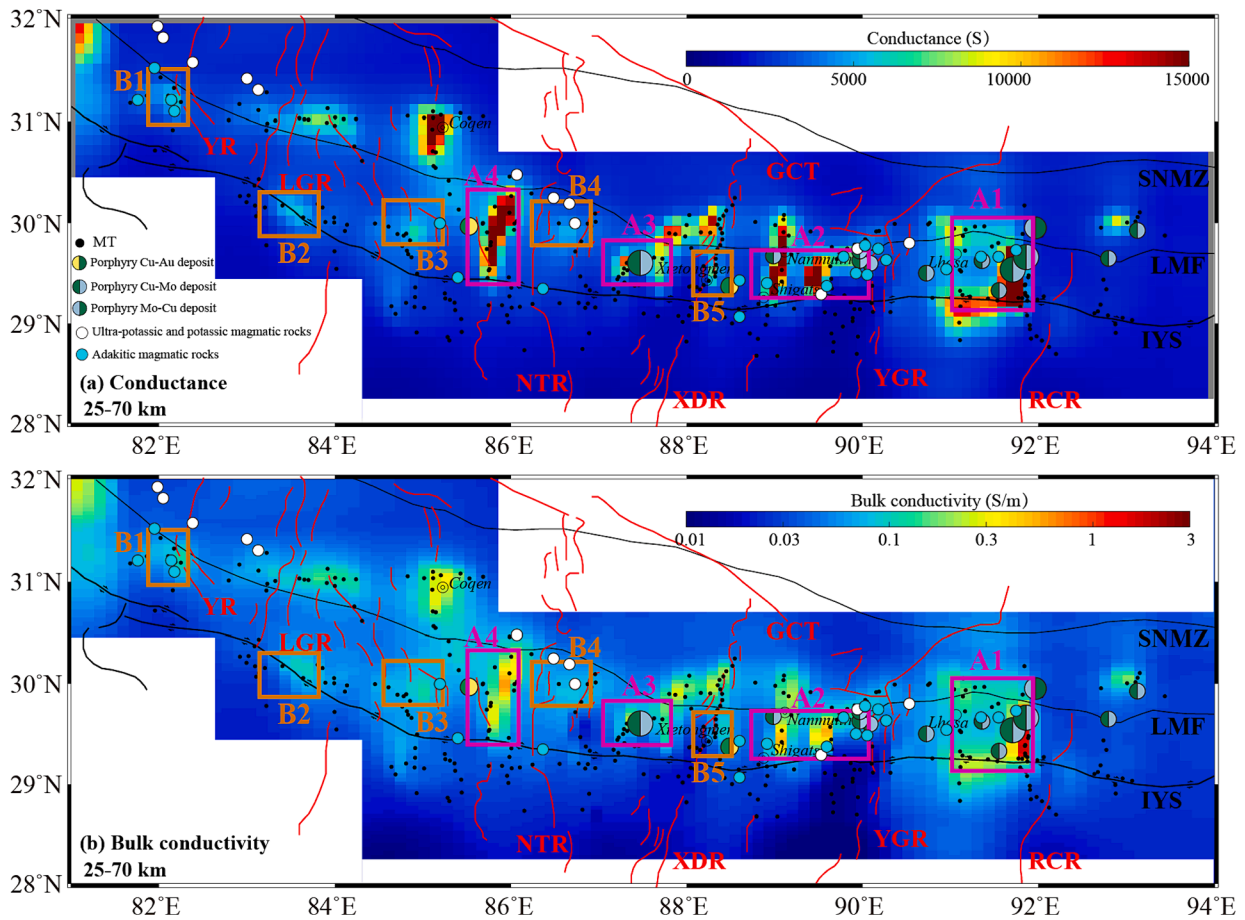
$$(4)$$

**Fig. 8.** Maps of (a) Conductance and (b) Bulk conductivity at depths 25–70 km. High-conductance (high bulk conductivity) areas are marked with boxes. A1, A2, A3 and A4 are marked as the conductive zones with the conductance of more than 10,000 S (pink box), which B1, B2, B3, B4 and B5 are marked as the conductive zones with the conductance of more than 5,000 S (orange box). Refer to Fig. 1 for labels. (For interpretation of the references to colour in this figure legend, the reader is referred to the web version of this article.)

$$\log \sigma_{melt}^{rhyolite} = 2.983 - 0.0732w - \frac{3528 - 233.8w + (763 - 7.5w^2)P}{T} \quad (5)$$

where $w$ is the water content in wt%, $T$ is temperature in K, $P$ is pressure in GPa.

We estimate the conductivity of andesite melt (Equation 4; 60.8 wt% $SiO_2$) and rhyolite melt (Equation 5; 75.7 wt% $SiO_2$) under specific temperature (950℃; Sun et al., 2013) and pressure conditions (1.32 GPa; Bai et al., 2013). We find the conductivity of silicate melts can be in the range of 1–12 S/m, assuming a water content of 5–8 wt% (cf. Sheng et al., 2022). The rock matrix has a resistivity of approximately 450 Ω·m in the southern Lhasa terrane (Jin et al., 2022). Computations show that when the pure melt conductivity is 12 S/m (i.e., the maximum), melt fractions of at least 20 % are needed to explain the bulk conductivity of A1 and A2 and melt fractions of more than 5 % are needed for A3 and A4 (Fig. 9a).

The high melt fractions estimated for A1 and A2 are similar to previous results (Sheng et al., 2021,2022; Jin et al., 2022). However, high melt fractions are not compatible with the observed low velocity variation (e.g., Huang et al., 2020). Silicate melts in combination with (alkali-bearing) fluids may be orders of magnitude more conductive than the surrounding rocks in a magmatic-hydrothermal system (e.g., Klumbach & Keppler, 2020; Sheng et al., 2023; Unsworth et al., 2023). Therefore, the alkali-bearing fluids can have a significant contribution to explaining conductivity anomalies in the crust.

### 4.2. Volume fraction of alkali-bearing aqueous fluids

Sodium chloride (NaCl) is the main salt component found in crustal and shallow subduction zone fluids, whereas in mantle fluids it is potassium chloride (KCl) (Vlasov & Keppler, 2022). The alkaline content of partial melt is known to increase the conductivity (e.g., Vlasov & Keppler, 2022, and references therein). However, potassic volcanism in the region (Chen et al., 2017; Liu et al., 2021; Fig. 1a) indicates that $KCl–H_2O$ fluids derived from the upper mantle could have migrated upwards to shallow depths. The K/Na ratio at different depths varies (because of changing relative incompatibility; see Ni et al., 2015), which has an influence on the electrical conductivity; however, no petrophysical experiment has yet adequately discussed this issue in a quantitative way. Therefore, $H_2O–NaCl$ fluids and $H_2O–KCl$ fluids are assumed to be alkali-bearing fluids separately in this study, as it is unclear how to properly combine them.

We use the model of Guo & Keppler (2019) to estimate the conductivities of NaCl-bearing aqueous fluids (under specific temperature and pressure conditions). The equation is written as:

$$\log \sigma = -0.919 - \frac{872.5}{T} + 7.61 \log \rho + 0.852 \log c + \log \Lambda_0(T, \rho) \quad (6)$$

$$\log \sigma = -0.919 - \frac{872.5}{T} + 7.61 \log \rho + 0.852 \log c + \log \Lambda_0(T, \rho) \quad (6)$$

$$\Lambda_0(T, \rho) = 1573 - 1212\rho + \frac{537062}{T} - \frac{208122721}{T^2} \quad (7)$$
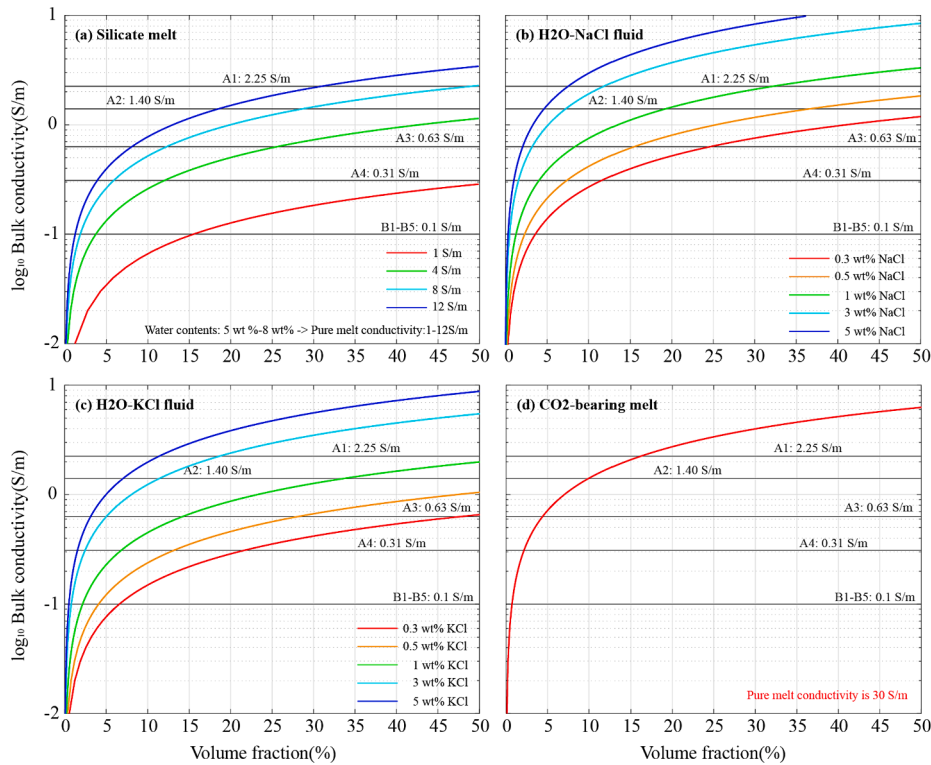
**Fig. 9.** Relationship between bulk conductivity and volume fraction of melts or fluids. (a) Silicate melts with varying water contents. (b) NaCl-bearing aqueous fluids with different salinities. (c) KCl-bearing aqueous fluids with different salinities. (d) $CO_2$ and $H_2O$-bearing melt. Conditions: T = 950 °C, P = 1.33GPa.

where $\sigma$ is the conductivity in S/m, $T$ is temperature in K, $c$ is NaCl concentration in wt%, $\rho$ is the density of pure water (in g/cm$^3$) at given pressure and temperature, and $\Lambda_0$ is the molar conductivity of NaCl in water at infinite dilution (in S·cm$^2$·mol$^{-1}$).

Then, we use the model of Vlasov & Keppler (2022) to estimate the conductivities of the KCl-bearing aqueous fluids (under specific temperature and pressure conditions). The equation is written as:

$$\log\sigma = -2.03 + \frac{25}{T} + 0.923\log c + 0.990\log\rho + \log \Lambda_0(T,\rho) \qquad (8)$$

$$\Lambda_0(T,\rho) = 1377 - 1082\rho - \frac{688300}{T} - \frac{247100000}{T^2} \qquad (9)$$

where $\sigma$ is the conductivity in S/m, $T$ is temperature in K, $c$ is KCl concentration in wt%, $\rho$ is the density of pure water (in g/cm$^3$) at given pressure and temperature, and $\Lambda_0$ is the molar conductivity of KCl in water at infinite dilution (in S·cm$^2$·mol$^{-1}$).

The results show that, under the condition of T = 950°C (1224.15 K) and P = 1.32 GPa, the $H_2O$–NaCl fluids (Equations 6 and 7) may have conductivities ranging from 1.7 to 46.5 S/m, assuming 0.3–5 wt% NaCl (Fig. 9b), and the $H_2O$–KCl fluids (Equations 8 and 9) have conductivities ranging from 2.3 to 30.8 S/m, assuming 0.3–5 wt% KCl (Fig. 9c), at 1.32GPa (average pressure) and 950 °C (average temperature). It is clear that the ranges of conductivity for fluids are larger than those for melts (Fig. 9 b, c). For a concentration > 3 wt% of NaCl or KCl, the conductivity possible for $H_2O$–NaCl or $H_2O$–KCl fluids is much higher than the maximum possible for silicate melts. Because the electrical conductivity is more sensitive to the presence of Na$^+$ and K$^+$ (alkali ions) than the seismic velocity (e.g., Naif et al., 2021, and others), a low volume of saline fluids can make a significant difference to bulk conductivity but a negligible or small difference to seismic velocity. Therefore, considering water contents in the melts in the southern Lhasa terrane (Sheng et al., 2022; references therein), alkali-rich fluids in combination with melts must exist in the very high-conductance areas (Sheng et al., 2023).

### 4.3. Volume fraction of CO$_2$-bearing melts

In the shallow area of the subduction zone, carbon dioxide ($CO_2$) can be released in the upwelling fluids or melts because of the decarbonization of the large-scale subducted lithospheric plate (Plank & Manning, 2019). Geochemical analysis of hot springs distributed in the southern Lhasa terrane (Klemperer et al., 2022) indicate the possibility of deep carbon cycling in this zone. Furthermore, carbon dioxide played an essential role in the carbonate alteration zone during the mineralization and the formation of potassic and ultra-potassic volcanic rocks in the region (Xu et al., 2022). The conductivity may be low (0.01 S/m) when carbon dioxide exists as magmatic volatiles (e.g., Samrock et al., 2021), however, the carbonate groups ($CO_3^{2-}$) in the melt can increase the conductivity in the mixed system.

We use the model of Guo et al. (2021) to estimate the conductivities of $CO_2$ and $H_2O$-bearing nephelinitic melt (under specific temperature and pressure conditions). The equation is written as:

$$\mathrm{In}\sigma = \mathrm{In}\sigma_o - \frac{\Delta E + P\Delta V}{RT} \qquad (10)$$

where $\sigma$ is the conductivity in S/m, $T$ is temperature in K, P is pressure in GPa, R is the universal gas constant (8.3145 J K$^{-1}$ mol$^{-1}$), $\sigma_o$ is the pre-exponential factor, $\Delta E$ is the activation energy, and $\Delta V$ is the activation volume. When the content of $CO_2$ is more than 6 wt%, $\mathrm{In}\sigma_o, \Delta E$ and $\Delta V$ can be 10.5 S/m, 75.2 kJ/mol, and 7.3 cm$^3$/mol, respectively.

Guo et al. (2021) reported that more than 6 wt% $CO_2$ can have a positive effect on conductivity, and the conductivity of the $CO_2$ and $H_2O$-bearing melt can be approximately 30 S/m at 1.32 GPa and 950 °C (Equation 10). The result shows that the volume of the $CO_2$-free (or $CO_2$ < 6 wt%) melt is at least three times that of the $CO_2$-$H_2O$-bearing ($CO_2$ > 6 wt%) melt in order to produce the same bulk conductivity (Fig. 9 d), using a two-phase system (solid and liquid). Again, requiring a lower volume of the fluid phase can help reconcile the results with the observed minimal decrease of seismic velocity.

## 4.4. Forming mechanism of the conductive zones

Alkali-rich fluid in the crust is largely chlorate aqueous fluid, which is related to the chlorine volatile in the material circulation between Earth sub-systems (e.g., Zhao et al., 2023). When alkali-rich fluids exist in the mid-lower crust, and when the mid-lower crust is hot, it is likely that partial melt also exists (e.g., Unsworth et al., 2005). Besides the free alkali-bearing fluid in the crust, the miscibility of silicate melts and aqueous (saline) fluids can be equivalent to the alkali-rich melt. Previous studies showed that $CO_2$ has an extremely low solubility in silicate minerals, but has a much higher solubility in alkali-rich melts (e.g., Guo et al., 2021). Guo et al. (2021) also reported that when the $CO_2$ content is low (approximately $\leq 6$ wt%) in the melt, it may show a weak effect on conductivity. Therefore, the conductive zones A1–A4 are more likely to result from silicate melts with different contents of alkali metal ions and volatiles ($CO_2$ and Cl), whereas the conductive zones B1–B5 mainly result from (water-bearing) silicate melts (perhaps with small amounts of volatiles). This interpretation differs from previous ideas (Sheng et al., 2022; Jin et al., 2022).

Furthermore, Ni et al. (2017) reported that under the high-temperature and high-pressure conditions in subduction zones, the miscible condition of silicate melts and aqueous (saline) fluids is enhanced to form supercritical aqueous fluids, the conductivity of which is higher than that of water-rich silicate melts and water-rich (alkali-bearing) fluids. These supercritical aqueous fluids can play an essential role in the circulation and migration of materials, mineralization, and intermediate-anatectic magmas. Hou et al. (2020) reported that supercritical aqueous fluids probably contributed to the evolution of the MPCDs in the Qulong-Jima district. Therefore, the influence of a small number of supercritical aqueous fluids on the conductivity of areas A1 and A2 may not be excluded.

Previous studies have reported that at least 5 % melt can result in one order of magnitude strength reduction, which can reduce the viscosity of rocks (e.g., Unsworth et al., 2005). In combination with the observed velocity reductions in this area (Huang et al., 2020) and crustal motion (Gan et al., 2007), it is interpreted that at least 10 % melt volume is required to explain anomalies A1–A4, and at least 5 % melt volume may contribute to the bulk conductivity in anomalies B1–B5.

The electrical structure at depths of 20 km is characterized by discrete conductive zones, some of which have a connection to conductive zones below in the mid-lower crust. In contrast, the electrical structure at depths of more than 30 km is characterized by extensive high-resistivity zones. Sun et al. (2013) revealed that the temperature at depths of ~ 20 km in the upper crust between longitudes 87°E and 92°E can be more than 650℃; whereas to the west between 82°E and 87°E, it is ~ 580℃ or less. These conductive zones are more likely to result from saline fluids with a small volume of melts, which may be related to cooling and crystallization of magmas after multi-period magmatic activities.

## 5. Discussion

### 5.1. Relationship of the conductive zones and material source of the MPCDs

On the whole, the MPCDs are mainly located above the zones of high-conductivity and very high-conductance (>10,000S; areas A1, A2, and A3) and near their edges (Fig. 7). The ultra-large deposits (Qulong and Jiama) and most of the large deposits (e.g., Nuri, Chongmuda, Bairong, Tinggong, and Chongjiang) in the eastern Gangdese metallogenic belt are distributed directly above or in the vicinity of A1 and A2, while the Zhunuo porphyry Cu deposit is above A3 (Fig. 7). On one hand, the activity and enrichment capacity of the metal ions is much higher in alkali rich melts/fluids (e.g., Wang et al., 2020), and the concentration of the Cl⁻ ions also increases the distribution ratio of metal ions in the fluid (including melt) (Poty et al., 1972; Zhao et al., 2023); on the other

hand, there is a contribution from the carbonate contact zone and carbon dioxide on the mineralization of the MPCDs. Hou et al., (2020,2023) further reported that the high-salinity liquid phase and low-density supercritical vapor-phase fluid can transport metals and form porphyry copper deposits with large-scale hydrothermal alteration. The system of alkali-rich volatile-rich partial melting in the conductive zones A1, A2, and A3 can correspond with the geochemical data, and may facilitate the super-enrichment of metals.

Although the Hf isotope results (Hou et al., 2015) show that areas A1, A2, and A3 have high εHf and low $T_{DM}^C$ values (within the juvenile lower crust), the peak of the Nd isotopic data occurs between longitudes 90°E and 92°E (Luo et al., 2022; Xu et al., 2022), which corresponds well with A1 and A2. Maps of the Moho depth show a thicker crust below A1 and A2 than in other areas (Li et al., 2013). It is possible that the thickened crust effectively resisted large-scale eruptions of ore-bearing magmas, which directly contributed to the formation of large-scale, stable magma chambers in the upper crust (Hou & Cook, 2009). This is intriguing because the re-melting of arc-related cumulates at the bottom of the crust which formed during lower crustal growth and thickening most likely played an essential role in the release of metals (Hou et al., 2015; Comeau et al., 2022). With the alkali-rich volatile-rich magmatic-hydrothermal fluids in the conductive areas A1 and A2, it is a possible reason why most large and ultra-large Cu polymetallicpolymetallic deposits (such as Qulong and Jima) discovered at present are gathered in this region (Fig. 8).

Previous studies showed that the subduction angle of the Indian Plate is shallower to the west of longitude 88°E than to the east (e.g., Chen et al., 2015; Guo et al., 2018; Sheng et al., 2019). This implies that the location of the plunging subduction of the Indian Plate in the west (beneath A3 and A4) is farther north than in the east (beneath A1 and A2), and the tearing of the Indian Plate may occur beneath the N-S-trending grabens or rifts (e.g., Bian et al., 2020). Although from the crustal electrical structure it is difficult to sketch the tearing of the subducted Indian Plate at depth, the variation of the northern boundaries of the resistive zone in the south along the IYS can indicate differential subduction of the Indian Plate. Importantly, it has been reported that a torn slab, subducted at moderate angle, is a key factor for the mineralization of the MPCDs (Hou et al., 2023). Therefore, east of 88°E (A1 and A2), both partial melting of the lithospheric mantle resulting from upwelling of the asthenosphere and metasomatism of the subducted Indian Plate and mantle wedge formed masses of mantle-derived thermal materials, and subsequently partial melting of a subduction-modified lower crust mixed with melt derived from the lithospheric mantle at the source depth (e.g., Xu et al., 2022). West of 88 °E, the impedance of thermal materials at depth because of the northward subduction of the Indian Plate (e.g., Hou et al., 2023) may cause tectonic thermal events to contribute to the variation of conductivity. This may be a possible reason why MPCDs are sparse near area A3 (Zhunuo).

In comparison, area A4 is adjacent to the Niyima-Tingri rift (NTR), including the Triassic Luerma subduction-related porphyry Cu-Au deposit that has been recently discovered at the western edge and some ultrapotassic and potassic rocks exposed in the north (Xu et al., 2022). No MPCDs (collision-related type) are located in A4. The Nd-Hf isotope (εNd and εHf: −2 to 2) and oxygen isotope ($\delta^{18}$O: ~6‰) results (Hou et al., 2023) show that this area is different from other areas with ancient crust (low εNd, negative εHf and high $\delta^{18}$O) west of the Zhunuo region (approximately longitude 87.5°E). It is more likely that the conductive zone A4 is related to multi-stage magmatic activities in this region.

As mentioned above, combined with the coupling relation between geological, geochemical, and geophysical data, large and ultra-large MPCDs are spatially coincident with conductive zones and areas of very high conductance located in the mid-lower crust. The former may represent partial melting of juvenile lower crust (high εHf values, low DMc values; Hou et al., 2015) that resulted from underplating of mantle-derived melt and migration channels of magmatic-hydrothermal fluids;

the latter may represent the influence of alkali-rich $CO_2$-$H_2O$ bearing magmatic-hydrothermal fluids on the migration and concentration of metal ions (e.g., Wang et al., 2015; Comeau et al., 2021).

What's more, Tang et al. (2011) discussed how deep-seated magma ascended repeatedly into the crust to form large-volume multi-stage magma chambers at various depths. The MPCDs are congruent with some discrete conductive zones in the upper crust, which are probably related to the electrical trace of the ancient magma chambers in the upper crust. Therefore, the results reveal the magma source area of anatexis in the lower crust, large-scale deep-seated magma chambers in the mid-crust, and some multi-stage magma chambers at different depths in the upper crust that resulted from emplacement of deep-seated magma along complex fracture systems (Fig. 10). Thus, the alkali-rich volatile-rich magmatic-hydrothermal fluids play an essential role during the mineralization of the collision-related MPCDs in the Tibetan Plateau.

Taken together, the results indicate that the tectonic dynamics related to the plunging subduction (east of 88°E) and/or tearing of the Indian Plate (beneath the north–south-trending rifts) facilitated crust-mantle interaction and is responsible for the occurrence of alkali-rich volatile-rich partial melting because of the surplus of mantle-derived thermal materials, which can drive the formation of collision-related porphyry Cu deposits (Zheng et al., 2020).

## 5.2. Influence of the crustal viscosity on the MPCDs

Previous studies reported that if the volume of partial melt or fluid reaches values greater than about 5 %, it can lower the effective viscosity substantially (e.g., Unsworth et al., 2005; Rosenberg and Handy, 2005). For example, a melt fraction of 5 %–10 % may reduce the viscosity by an order of magnitude and a melt fraction of about 20 % may reduce the viscosity by two orders of magnitude (Jin et al., 2022, and references therein). Estimates for the volume fraction of melts or fluids

at depths of 25–70 km are therefore compatible with a reduced effective viscosity in the mid-lower crust in areas A1–A4, possibly by more than an order of magnitude.

The MT method is sensitive to fluids and has a dependence on temperature; these properties make it a very promising proxy for estimating mechanical strength variations in the lithosphere. Because the electrical resistivity is sensitive to the quantity and composition of fluids as well as to the temperature, Liu and Hasterok (2016) showed that it can be used to estimate mechanical strength variations in the lithosphere. A simple scaling relation to convert from electrical resistivity to viscosity is given as:

$$\frac{\eta_{eff}}{\eta_0} = C_0 \left( \frac{\rho}{\rho_0} \right)^{C_1} \tag{11}$$

where $\eta_{eff}$ represents the effective viscosity, and $\eta_0$ represents the reference viscosity, $\rho$ is the measured resistivity, $\rho_0$ is the reference resistivity, and $C_0$ and $C_1$ are scaling coefficients (Liu and Hasterok, 2016). Based on the study of Sheng et al. (2022), $C_0$ and $C_1$ can be set as 2.0 and 1.1 in the southern Lhasa terrane. Using this simple relationship, the estimated variation of effective viscosity across the study area (Fig. 11) is shown to be similar to that predicted from the volume fraction estimates in areas A1–A4.

Besides the fluid/melt source region and the specific magmatic evolution, the geodynamic history, regional tectonics, and structural architecture of the region also control the metallogenesis of porphyry Cu deposits (e.g., Hou et al., 2020; Comeau et al., 2021, 2022; see also Huston et al., 2016). Wang et al. (2021) reported that prominent tearing in the Indian lithosphere, sub-parallel to a rift zone (Yadong-Gulu rift), played an important role in the tectono-thermal anomalies and the formation of MPCDs between longitudes 90°E and 92°E during the Miocene. The large conductive zones in the mid-lower crust may result in the decoupling of the brittle upper crust from the lower lithosphere and thereby contribute to surface deformation (Sheng et al., 2021, 2022;
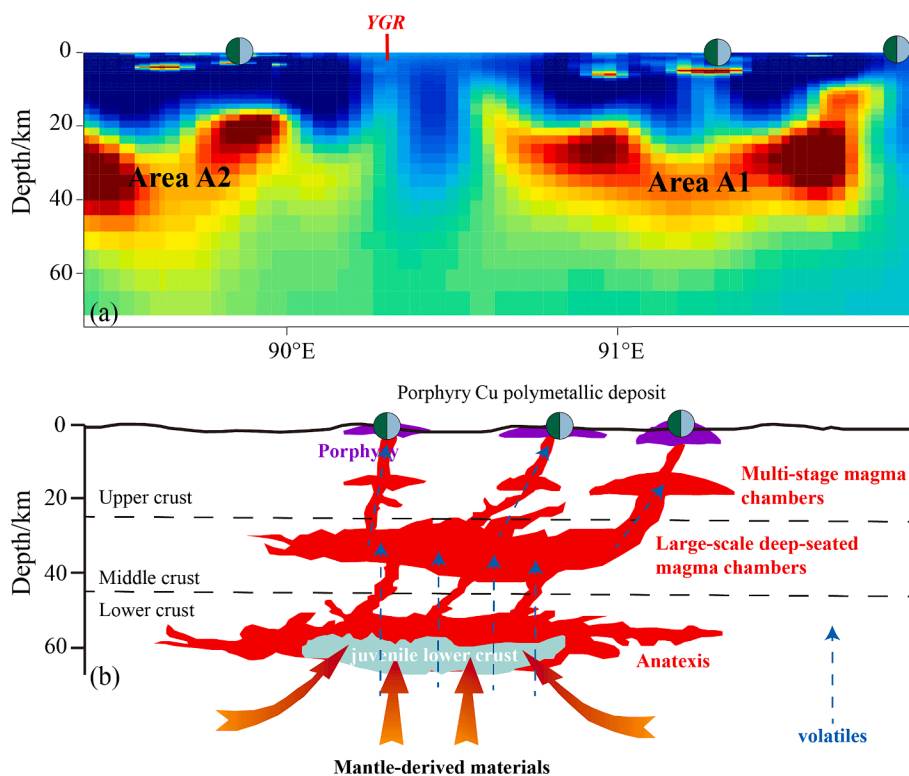


**Fig. 10.** Model section and cartoon for interpretation. (a) Cross-section of the electrical structure. Location is pink line in Fig. 7c. (b) Simplified sketch of the proposed metallogenic evolution of the MPCDs based on the electrical structure (see also: Sheng et al., 2022; Xu et al., 2023). Not to scale. Refer to Fig. 1 for labels. (For interpretation of the references to colour in this figure legend, the reader is referred to the web version of this article.)
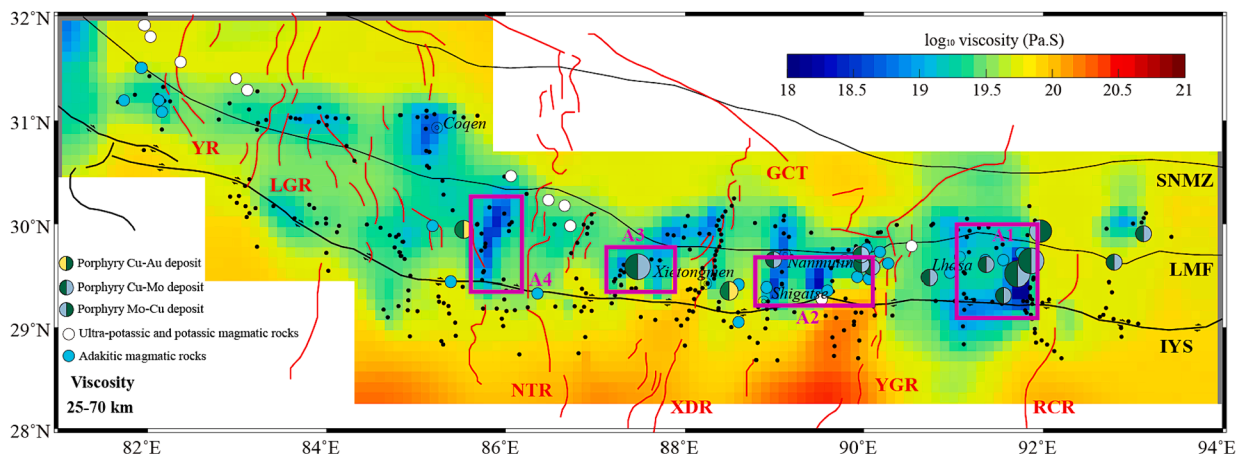
**Fig. 11.** Viscosity of the middle-lower crust (25–70 km). Viscosity is estimated by applying the scaling relation proposed by Liu and Hasterok (2016). The coefficients values are $C_0 = 2.0$, and $C_1 = 1.1$ (referring to Sheng et al., 2022). Refer to Fig. 1 for labels.

Jin et al., 2022). Meanwhile, in regions in which the stress was concentrated, the N-S-trending grabens or rifts were formed, although, interestingly, the formation age of the MPCDs is slightly earlier than that of the rifts (e.g., Hou et al., 2015; Bian et al., 2020). The development of the MPCDs following mineralization may be influenced by these weakened zones in the mid-lower crust.

## 6. Summary

A magnetetolluric dataset covering a polymetallic belt in the southern Tibetan Plateau is used to generate a 3-D electrical resistivity model. Zones with very high conductance (>10,000 S) are identified in the mid-lower crust. These zones are spatially coincident with the location of Miocene porphyry copper deposits. We investigated the influence of partial melt and alkali metal ions on the conductivity and mineralization. We conclude that these conductive zones may result from alkali-rich volatile-rich magmatic-hydrothermal fluids, and processes related to them, including metasomatism and exsolution. This interpretation can not only reconcile the differences seen with large conductivity variations but small velocity variations, but also explain the migration and concentration of metal ions in the magmatic-hydrothermal systems in this region, resulting in large and ultra-large deposits (e.g., Qulong and Jiama).The imaged electrical structure indicates a transcrustal mineral system including the magma source area of anatexis in the lower crust, partially molten zones in the mid-crust, and some multi-stage magma reservoirs at different depths in the upper crust. The conductive zones in the mid-lower crust also correspond with the location of N-S-trending rifts at the surface, which may influence the development of the mineral system, and large size of the deposits, by providing natural fluid-flow pathways or weaknesses within the lithospheric-scale architecture.

## Data availability statement

Model and data can be accessed from http://dx.https://doi.org/10.17632/rnvcgtfvyd.1.

## Declaration of competing interest

The authors declare that they have no known competing financial interests or personal relationships that could have appeared to influence the work reported in this paper.

## Data availability

No data was used for the research described in the article.

## Appendix A. Supplementary data

Supplementary data to this article can be found online at https://doi.org/10.1016/j.oregeorev.2024.106033.

## References

Bai, Z.M., Zhang, S., Braitenberg, C., 2013. Crustal density structure from 3D gravity modeling beneath Himalaya and Lhasa blocks, Tibet. J. Asian Earth Sci. 78 (12), 301–317. https://doi.org/10.1016/j.jseaes.2012.12.035.

Bian, S., Gong, J.F., Zuza, A.V., Yang, R., Tian, Y.T., Ji, J.Q., Chen, H.L., Xu, Q.Q., Chen, L., Lin, X.B., Chen, X.G., Tu, J.T., Xu, X.J., 2020. Late Pliocene onset of the Cona rift, eastern Himalaya, confirms eastward propagation of extension in Himalayan-Tibetan orogen. Earth Planet. Sci. Lett. 116383 https://doi.org/10.1016/j.epsl.2020.116383.

Caldwell, T.G., Bibby, H.M., Brown, C., 2004. The magnetotelluric phase tensor. Geophys. J. Int. 158, 457–469. https://doi.org/10.1111/j.1365-246X.2004.02281.x.

Chen, M., Niu, F., Tromp, J., Lenardic, A., Lee, C., Cao, W., et al., 2017. Lithospheric foundering and underthrusting imaged beneath Tibet. Nat. Commun. 8, 15659. https://doi.org/10.1038/ncomms15659.

Comeau, M.J., Becken, M., Kuvshinov, A., Demberel, S., 2021. Crustal architecture of a metallogenic belt and ophiolite belt: Implications for mineral genesis and emplacement from 3-D electrical resistivity models (Bayankhongor area, Mongolia). Earth Planets Space 73. https://doi.org/10.1186/s40623-021-01400-9.

Comeau, M.J., Becken, M., Kuvshinov, A., 2022. Imaging the whole-lithosphere structure of a mineral system — Geophysical signatures of the sources and pathways of ore-forming fluids. Geochem. Geophys. Geosyst. 23 (8), 18. https://doi.org/10.1029/2022GC010379.

Di, Q.Y., Zhang, K., Xue, G.Q., An, Z.G., Fu, G.M., Guo, W.B., Zhang, S.M., 2023. A top-down control on upper crustal inheritance on the south-eastern Tibetan Plateau. Tectonophysics 863, 229992. https://doi.org/10.1016/j.tecto.2023.229992.

Egbert, G.D., 1997. Robust multiple-station magnetotelluric data processing. Geophys. J. R. Astron. Soc. 136 (2), 475–496. https://doi.org/10.1111/j.1365-246X.1997.tb05663.x.

Egbert, G.D., Kelbert, A., 2012. Computational recipes for electromagnetic inverse problems. Geophys. J. Int. 189 (1), 251–267. https://doi.org/10.1111/j.1365-246X.2011.05347.x.

Gan, W., Zhang, P., Shen, Z.-K., Niu, Z., Wang, M., Wan, Y., et al., 2007. Present-day crustal motion within the Tibetan Plateau inferred from GPS measurements. J. Geophys. Res. 112, B08416. https://doi.org/10.1029/2005JB004120.

Guo, H., Keppler, H., 2019. Electrical conductivity of Nacl-bearing aqueous fluids to 900 °C and 5 GPa. J. Geophys. Res.: Solid Earth 124 (2–3). https://doi.org/10.1029/2018JB016658.

Guo, X., Zhang, L., Behrens, H., Ni, H., 2016. Probing the status of felsic magma reservoirs: constraints from the P-T-H2O dependences of electrical conductivity of

rhyolitic melt. Earth Planet. Sci. Lett. 433, 54–62. https://doi.org/10.1016/j. epsl.2015.10.036.

Guo, X., Li, B., Ni, H., Mao, Z., 2017. Electrical conductivity of hydrous andesitic melts pertinent to subduction zones. J. Geophys. Res. Solid Earth 122, 1777–1788. https:// doi.org/10.1002/2016JB013524.

Guo, X., Wang, Q., Li, B., Zha, X.-P., Gong, B., Ni, H., 2021. Electrical conductivity of $CO_2$ and $H_2O$ bearing nephelinitic melt. e2020JB019569 J. Geophys. Res. Solid Earth 126. https://doi.org/10.1029/2020JB019569.

Hashin, Z., Shtrikman, S., 1962. A variational approach to the theory of the effective magnetic permeability of multiphase materials. J. Appl. Phys. 33 (10), 3125–3131. https://doi.org/10.1063/1.1728579.

Hill, G.J., Roots, E.A., Frieman, B.M., Haugaard, R., Craven, J.A., Smith, R.S., Snyder, D. B., Zhou, S., Sherlock, R., 2021. On Archean craton growth and stabilisation: Insights from lithospheric resistivity structure of the Superior Province. Earth Planet. Sci. Lett. 562, 116853 https://doi.org/10.1016/j.epsl.2021.116853.

Hou, Z.Q., Duan, L., Lu, Y., Zheng, Y., Zhu, D., Yang, Z., Yang, Z., Wang, B., Pei, Y., Zhao, Z., McCuaig, T.C., 2015. Lithospheric architecture of the Lhasa terrane and its control on ore deposits in the Himalayan-Tibetan orogen. Econ. Geol. 110, 1541–1575. https://doi.org/10.2113/econgeo.110.6.1541.

Hou, Z.Q., Yang, Z.M., Wang, R., Zheng, Y.C., 2020. Further discussion on porphyry Cu-Mo-Au deposit formation in Chinese mainland. Earth Sci. Front. 27 (2), 020–044. https://doi.org/10.13745/j.esf.sf.202.3.8.

Hou, Z.Q., Wang, R., Zhang, H.J., Zheng, Y.C., Jin, S., Thybo, H., Weinber, R.F., Xu, B., Yang, Z.M., Hao, A.W., Gao, L., Zhang, L.T., 2023. Formation of giant copper deposits in Tibet driven by tearing of the subducted Indian plate. Earth Sci. Rev. Vol. 243, 104482.

Huang, S.Y., Yao, H., Lu, Z., Tian, X., Zheng, Y., Wang, R., Luo, S., Feng, J.K., 2020. High-Resolution 3-D shear wave velocity model of the Tibetan plateau: implications for crustal deformation and porphyry cu deposit formation. J. Geophys. Res. Solid Earth 125. https://doi.org/10.1029/2019JB019215.

Huston, D.L., Mernagh, T.P., Hagemann, S.G., Doublier, M.P., Fiorentini, M., Champion, D.C., Jaques, A.J., Czarnota, K., Cayley, R., Skirrow, R., Bastrakov, E., 2016. Tectono-metallogenic systems–The place of mineral systems within tectonic evolution, with an emphasis on Australian examples. Ore Geol. Rev. 76, 168–210. https://doi.org/10.1016/j.oregeorev.2015.09.005.

Jin, S., Sheng, Y., Comeau, M.J., Becken, M., Wei, W., Ye, G., Zhang, L.T., Dong, H., 2022. Relationship of the crustal structure, rheology, and tectonic dynamics beneath the Lhasa-Gangdese terrane (southern Tibet) based on a 3-D electrical model. e2022JB024318 J. Geophys. Res. Solid Earth 127. https://doi.org/10.1029/ 2022JB024318.

Kelbert, A., Meqbel, N., Egbert, G.D., Tandon, K., 2014. ModEM: a modular system for inversion of electromagnetic geophysical data. Comput. Geosci 66, 40–53. https:// doi.org/10.1016/j.cageo.2014.01.010.

Klemperer, S.L., Zhao, P., Whyte, C.J., Darrah, T.H., Crossey, L.J., Karlstrom, K.E., Liu, T. Z., Winn, C., Hilton, D.R., Ding, L., 2022. Limited underthrusting of India below Tibet: &sup3; He/4He analysis of thermal springs locates the mantle suture in continental collision. Proc. Natl. Acad. Sci. USA 119 (12), 1–7. https://doi.org/ 10.1073/pnas.2113877119.

Klumbach, S., Keppler, H., 2020. Electrical conductivity of HCl–bearing aqueous fluids to 700°C and 1 GPa. Contrib. Miner. Petrol. 175, 114. https://doi.org/10.1007/ s00410-020-01754-5.

Li, Y.H., Gao, T.M., Wu, Q.J., 2013. Crustal thickness map of the Chinese mainland from teleseismic receiver functions. Tectonophysics 611. https://doi.org/10.1016/j. tecto.2013.11.019.

Liu, B.R., Dai, J.G., Shen, J., Xu, S., Han, X., 2021. Evidence for deep processes from the Miocene potassic rock: dynamic subsidence and uplift of the India-Asia suture zone. Lithos 388–389, 106061. https://doi.org/10.1016/j.lithos.2021.106061.

Liu, L., Hasterok, D., 2016. High-resolution lithosphere viscosity and dynamics revealed by magnetotelluric imaging. Science 353 (6307), 1515–1519. https://doi.org/ 10.1126/science.aaf6542.

Lü, Q.T., Meng, G.X., Zhang, K., Liu, Z.D., Yan, J.Y., Shi, D.N., Han, J.G., Guo, X.J., 2021. The lithospheric architecture of the lower Yangtze metallogenic belt, east China: insights into an extensive Fe–Cu mineral system. Ore Geol. Rev. https://doi.org/ 10.1016/j.oregeorev.2021.103989.

Luo, C.H., Wang, R., Weinberg, R.F., Hou, Z.Q., 2022. Isotopic spatial-temporal evolution of magmatic rocks in the Gangdese belt: Implications for the origin of Miocene post-collisional giant porphyry deposits in southern Tibet. Geol. Soc. Am. Bull. 1/2):134 https://doi.org/10.1130/B36018.1.

Naif, S., Selway, K., Murphy, B.S., Egbert, G., Pommier, A., 2021. Electrical conductivity of the lithosphere-asthenosphere system. Phys. Earth Planet. In. 313 (1), 106661 https://doi.org/10.1016/j.pepi.2021.106661.

Ni, H.W., Hui, H., Steinle-Neumann, G., 2015. Transport properties of silicate melts. Rev. Geophys. 53 (3), 715–744. https://doi.org/10.1002/2015RG000485.

Ni, H.W., Zhang, L., Xiong, X., Mao, Z., Wang, J., 2017. Supercritical fluids at subduction zones: evidence, formation condition, and physicochemical properties. Earth Sci. Rev. 167, 62–71. https://doi.org/10.1016/j.earscirev.2017.02.006.

Plank, T., Manning, C.E., 2019. Subducting carbon. Nature 574, 343–352. https://doi. org/10.1038/s41586-019-1643-z.

Poty, B., Holland, H.D., Borcsik, M., 1972. Solution-mineral equilibria in the system mgo-sio2-h2o-mgcl2 at 500°c and 1 kbar. Geochim. Cosmochim. Acta 36 (10), 1101–1113. https://doi.org/10.1016/0016-7037(72)90094-4.

Rosenberg, C.L., Handy, M.R., 2005. Experimental deformation of partially melted granite revisited: implications for the continental crust. J. Metam. Geol. 23 (1), 19–28. https://doi.org/10.1111/j.1525-1314. 2005.00555.x.

Samrock, F., Grayver, A.V., Bachmann, O., Karakas, Z., Saar, M.O., 2021. Integrated magnetotelluric and petrological analysis of felsic magma reservoirs: insights from Ethiopian rift volcanoes. Earth Planet. Sci. Lett. 559, 10.31223/X5Q600.

Sheng, Y., Jin, S., Wei, W.B., Ye, G.F., Dong, H., Zhang, L.T., Liang, H.D., Lu, Z.W., 2019. Lithospheric electrical structure in the central Tibetan Plateau and its tectonic significance. J. Asian Earth Sci. 184 https://doi.org/10.1016/j.jseaes.2019.103996.

Sheng, Y., Jin, S., Comeau, M.J., Dong, H., Zhang, L.T., Lei, L.L., Li, B.C., Wei, W.B., Ye, G.F., Lu, Z.W., 2021. Lithospheric structure near the northern Xainza-Dinggye Rift, Tibetan Plateau – implications for rheology and tectonic dynamics. J. Geophys. Res.: Solid Earth. https://doi.org/10.1029/2020JB021442.

Sheng, Y., Jin, S., Comeau, M.J., Becken, M., Dong, H., Zhang, L.T., Wei, W.B., Ye, G.F., 2022. Controls on the metallogenesis of the Lhasa-Mozugongka district, Gangdese Belt, Tibetan Plateau: Constraints on melt distribution and viscosity from the 3-D electrical structure of lithosphere. Ore Geol. Rev. https://doi.org/10.1016/j. oregeorev.2022.104881.

Sheng, Y., Jin, S., Comeau, M.J., Hou, Z.Q., Becken, M., Dong, H., Zhang, L.T., Wei, W.B., Ye, G.F., 2023. Evidence for partial melting and alkali-rich fluids in the crust from a 3-D electrical resistivity model in the vicinity of the Coqen region, western Lhasa terrane, Tibetan Plateau. Earth Planet. Sci. Lett. 118316 https://doi.org/10.1016/j. epsl.2023.118316.

Sun, Y.J., Dong, S.W., Zhang, H., Li, H., Shi, Y.L., 2013. 3D rheological structure of the continental lithosphere beneath China and adjacent regions. Chin. J. Geophys. 56 (5), 546–558. https://doi.org/10.1002/cjg2.20052.

Tang, Z.L., Qian, Z.Z., Jiang, C.Y., Yan, H.Q., Jiao, J.G., Liu, M.W., Xu, Z.H., Xu, G., Wang, Y.L., 2011. Trends of research in exploration of magmatic sulfide deposits and small intrusions metallogenic system. J. Earth Sci. Environ. 33 (1), 1–9. https://doi. org/10.3969/j.issn.1672-6561.2011.01.001.

Unsworth, et al., 2023. Crustal structure of the Lazufre volcanic complex and the Southern Puna from 3-D inversion of magnetotelluric data: Implications for surface uplift and evidence for melt storage and hydrothermal fluids. Geosphere 19 (5), 1210–1230. https://doi.org/10.1130/GES02504.1.

Unsworth, M.J., Jones, A.G., Wei, W., Marquis, G., Gokarn, S.G., Spratt, J.E., Team, 2005. Crustal rheology of the Himalaya and Southern Tibet inferred from magnetotelluric data. Nature 438 (7064), 78–81. https://doi.org/10.1038/ nature04154.

Vadoodi, R., Rasmussen, T.M., Smirnov, M., et al., 2021. Towards an understanding of mineral systems – contributions from magnetotelluric data from the Fennoscandian shield in northern Sweden. Tectonophysics 808, 228816.

Vlasov, K., Keppler, H., 2022. Electrical conductivity of KCl-H2O fluids in the crust and lithospheric mantle. e2022JB024080 J. Geophys. Res.: Solid Earth 127. https://doi. org/10.1029/2022JB024080.

Wang, R., Richards, J.P., Zhou, L.M., Hou, Z.Q., Stern, R.A., Creaser, R.A., Zhu, J.J., 2015. The role of Indian and Tibetan lithosphere in spatial distribution of Cenozoic magmatism and porphyry Cu–Mo deposits in the Gangdese belt, southern Tibet. Earth Sci. Rev. 150, 68–94. https://doi.org/10.1016/j.earscirev.2015.07.003.

Wang, R., Weinberg, R.F., Collins, W.J., Richards, J.P., Zhu, D.C., 2018. Origin of postcollisional magmas and formation of porphyry Cu deposits in southern Tibet. Earth Sci. Rev. 181, 122–143. https://doi.org/10.1016/j.earscirev.2018.02.019.

Wang, R., Weinberg, R.F., Zhu, D.C., Hou, Z.Q., Yang, Z.M., 2021. The impact of a tear in the subducted Indian plate on the Miocene geology of the Himalayan-Tibetan orogen. GSA Bull. https://doi.org/10.1130/B36023.1.

Wei, W.B., Unsworth, M., Jones, A., Booker, J., Tan, H.D., Nelson, D., Chen, L.S., Li, S.H., Solo, K., Bedrosian, P., Jin, S., Deng, M., Ledo, J., Kay, D., Roberts, B., 2001. Detection of widespread fluids in the Tibetan crust by magnetotelluric studies. Science 292 (5517), 716–719. https://doi.org/10.1126/science.1010580.

Wei, W.B., Jin, S., Ye, G.F., Deng, M., Jing, J.E., Unsworth, M.J., 2009. The conductivity structure and rheology of the lithosphere in the southern Tibet - the result of the study of ultra-wide band magnetotelluric sounding. Sci. China: (series d) 39 (11), 1591–1606. https://doi.org/10.1007/s11430-010-0001-7.

Xu, B., Hou, Z.Q., Griffin, W.L., O'Reilly, S.Y., Zheng, Y.C., Wang, T., Fu, B., Xu, J.F., 2022. In-situ mineralogical interpretation of the mantle geophysical signature of the Gangdese Cu-porphyry mineral system. Gondw. Res. 111, 53–63. https://doi.org/ 10.1016/j.gr.2022.07.005.

Yang, Z.M., Lu, Y.C., Hou, Z.Q., Chang, Z.S., 2015. High-Mg Diorite from Qulong in Southern Tibet: implications for the genesis of adakite-like intrusions and associated porphyry Cu deposits in collisional orogens. J. Petrol. 56 (2), 227–254. https://doi. org/10.1093/petrology/egu076.

Zhang, K., Lü, Q.T., Lan, X.Y., Guo, D., Wang, Q.N., Yan, J.Y., Zhao, J.H., 2021. Magnetotelluric evidence for crustal decoupling: Insights into tectonic controls on the magmatic mineral system in the Nanling-Xuancheng area, SE China. Ore Geol. Rev. 131 (2), 104045 https://doi.org/10.1016/j.oregeorev.2021.104045.

Zhang, K., Lü, Q.T., Man, Z.H., Lan, X.Y., Guo, D., Tao, L., Zhao, J.H., 2022. Electrical constraints on the deep setting and process of magma-mineral system in the Middle-Lower Reaches of Yangtze Metallogenic Belt. Acta Petrol. Sin. 38 (2), 573–583. https://doi.org/10.18654/1000-0569/2022.02.18.

Zhao, Y., Yu, J.X., Xu, B., Zhang, Y.F., Wang, Z.X., Hou, Z.Q., Kou, G.Y., Zhao, Z.Y., 2023. Zircon Hf-O and apatite Sr-O isotopes jointly reveal the origin and mineralization of the Miocene adakitic porphyries in the Gangdese belt. Ore Geol. Rev. 105536.

Zheng, Y.C., Liu, S.A., Wu, C.D., Griffin, W.L., Li, Z.Q., Xu, B., Yang, Z.M., Hou, Z.Q., O'Reilly, S.Y., 2018. Cu isotopes reveal initial Cu enrichment in sources of giant

porphyry deposits in a collisional setting. Geology. https://doi.org/10.1130/G45362.1.

Zheng, Y.C., Wu, C.D., Tian, S.H., Hou, Z.Q., Fu, Q., Zhu, D.C., 2020. Magmatic and structural controls on the tonnage and metal associations of collision-related porphyry copper deposits in southern Tibet. Ore Geol. Rev. 122, 103509 https://doi.org/10.1016/j.oregeorev.2020.103509.

Zhu, D.C., Wang, Q., Chung, S.L., Cawood, P.A., Zhao, Z.D., 2019. Gangdese magmatism in southern Tibet and India–Asia convergence since 120 Ma. In: Kingston, P.J., Searle, M.P. (Eds.), Himalayan Tectonics: A Modern Synthesis. Geological Society of London, Special Publication 483, p. 10.1144/SP483.14.